THz Quantum Semiconductor Devices

H. C. Liu[€], H. Luo, D. Ban, M. Wächter, C. Y. Song,
Z. R. Wasilewski, M. Buchanan, G. C. Aers, A. J. SpringThorpe
Institute for Microstructural Sciences, National Research Council, Ottawa K1A 0R6, Canada

J. C. Cao, S. L. Feng
State Key Laboratory of Functional Materials for Informatics, Shanghai Institute of Microsystem and Information Technology, Chinese Academy of Sciences, Shanghai 200050, China

B. S. Williams, Q. Hu
Department of Electrical Engineering and Computer Science and Research Laboratory of Electronics, Massachusetts Institute of Technology, Cambridge, Massachusetts 02139, USA

ABSTRACT

Terahertz (1 – 10 THz) quantum-well photodetectors and quantum-cascade lasers have been investigated. The design and projected detector performance are presented together with experimental results on several test devices, all working at photon energies below the optical phonons. Background limited infrared performance (BLIP) operations were observed for all samples (three in total) designed for different wavelengths. For lasers, a set of THz quantum-cascade lasers with identical device parameters except for the doping concentration has been studied. The δ-doping density for each period was varied from 3.2×10^{10} to 4.8×10^{10} cm^{-2}. We observed that the lasing threshold current increased monotonically with doping. Moreover, the measured results on devices with different cavity lengths provided evidence that the free carrier absorption caused waveguide loss also increased monotonically. Interestingly however, the observed maximum lasing temperature displayed an optimum at a doping density of 3.6×10^{10} cm^{-2}.

1. INTRODUCTION

Terahertz (THz) waves have attracted much recent attention.[1,2] The THz region is loosely defined as the range of frequencies from 1 to 10 THz (wavelengths from 30 to 300 μm or energies from 4.1 to 41 meV). Although many proof-of-concept experiments have been carried out, demonstrating potential applications of THz technologies,[1-3] the lack of compact and convenient THz generation and detection devices needs to be addressed before widespread applications become a reality. This paper summarizes our recent efforts in the research and development of both THz quantum-well photodetectors and quantum-cascade lasers (QCL).

2. THz QUANTUM-WELL PHOTODETECTORS

2.1. Design considerations

The approach taken here is to extend the wavelength coverage of quantum-well infrared photodetectors[4] (QWIP) into the THz region. QWIP materials are commonly GaAs/AlGaAs.[4] The high absorption by the optical phonons of GaAs makes the region of 34 – 36 meV (34 – 36 μm or 8 – 9 THz) inaccessible. The quantum-well design using GaAs/AlGaAs is well known for mid-infrared QWIPs.[4] In the THz region, if we apply the same principle of having the first excited state in resonance with the top of the barrier, the calculated optimum quantum-well parameters are shown in Fig. 1. The calculation is a simple one, using the one-parabolic-band effective-mass approximation. From Fig. 1, it is predicted that the THz frequency range of 1 – 8 THz is covered by QWIPs with low aluminum fractions.

[€] Electronic mail: h.c.liu@nrc.ca; Tel: 1 613 993 3895; Fax: 1 613 990 0202

ICO20: Materials and Nanotechnologies, edited by Wei Lu, Jeff F. Young,
Proc. of SPIE Vol. 6029, 602901, (2005) · 0277-786X/05/$15 · doi: 10.1117/12.667658

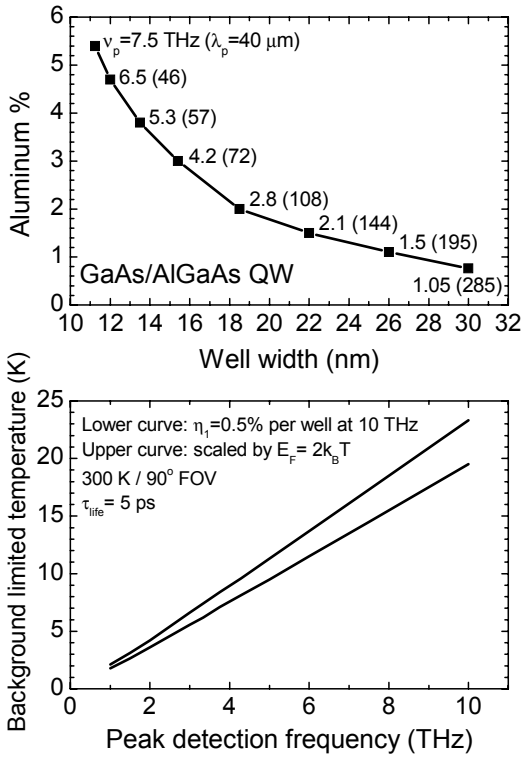

Figure 1: (Above) Calculated well width (L_w) and barrier aluminum alloy fraction (x) for an optimized GaAs/AlGaAs quantum well. The conduction band offset (barrier height V_b) relates to x by $V_b = 0.87 \times x$ (eV). The range covers the peak detection frequency υ_p (or wavelength λ_p) from 1.05 (285) to 7.5 THz (40 μm). (Below) Calculated temperature for background limited infrared performance versus peak detection frequency. The background temperature is 300 K and the field-of-view (FOV) full cone angle is 90 degrees. The upper curve has a lower absorption (by about 10 times) than the lower curve.

Any good detector must have a sufficiently high absorption. On one hand, a high doping is desirable for achieving high absorption; but on the other hand, high doping leads to a high dark current and low operating temperature. A trade-off[4] must therefore be made for a given application. For most applications, it is desirable to operate the detector under the background-limited condition. The temperature for achieving the background limited infrared performance (T_{blip}) is therefore an important figure-of-merit. Figure 1 also shows the calculated T_{blip} versus the peak detection frequency. The BLIP temperature is found by equating the calculated dark current and photocurrent caused by the background. The dark current is estimated by multiplying the mobile electron density and drift velocity (the "3D drift model" in Ref. [4]). The device parameters needed in this calculation are excited electron lifetime τ_{life} (taken as 5 ps), quantum-well period L_p (taken as 30 nm), and absorption efficiency per well η_1. For achieving the highest dark-current-limited detectivity, it has been established[4] that the well two-dimensional electron density n_{2D} should correspond to $E_F=2k_BT$, where the Fermi energy is given by $E_F=(\pi\hbar^2/m)n_{2D}$, m is the effective mass, and T is the operating temperature. For GaAs, $n_{2D} = 5 \times 10^{11}$ cm^{-2} corresponds to about 80 K and a one-well polarized absorption of about 0.5%.[4] If one follows the $E_F=2k_BT$ rule, the density would become very low for low temperatures (<<80 K), making the absorption also low. We therefore considered two cases in the lower part of Fig. 1. The upper curve uses the $E_F=2k_BT$ condition, while the lower curve starts with a higher absorption (using higher doping) η_1=0.5% at 10 THz, and reduces linearly down to 0.05% at 1 THz. The trade-off here is that if the operating temperature is desired to be as high as possible, the upper curve should be followed. Whereas, if a high absorption is needed one should use the lower curve, but requiring slightly more cooling. Reaching BLIP condition is necessary for detecting weak signals. In some applications involving a strong source such as a THz QCL, the requirement is different. Here as long as the dark current is lower than the signal photocurrent, the QWIP operating temperature may be raised.

The above analysis assumes that the tunneling contribution (such as, direct inter-well, scattering assisted, and hopping-like via deep-impurity levels in the barriers) is negligible. While some of the mechanisms are highly sample

dependent, such as those related to impurity and defect, the magnitude of direct inter-well tunneling is easy to estimate. Figure 2 shows the estimated tunneling current versus barrier thickness for three values of aluminum fraction x. The expression used for the estimate is $(evn_{2D}/L_w)D$, where $v=(2E_0/m)^{1/2}$, E_0 is the ground state energy, L_w is the well width, and D is the transmission coefficient calculated using the WKB approximation.

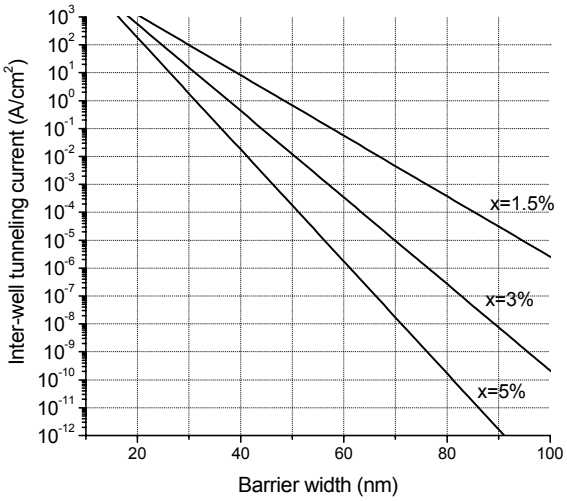

Figure 2: Estimated direct inter-well tunneling current versus barrier thickness for three cases of barrier aluminum fractions of x =1.5, 3, and 5%. Other parameters used for the estimate are E_0 = 4.3, 8.6, and 14 meV, n_{2D} = 0.3, 0.6, and 1.0 × 10^{11} cm^{-2}, and L_w = 22.0, 15.4, and 12.0 nm, for the three x values, respectively.

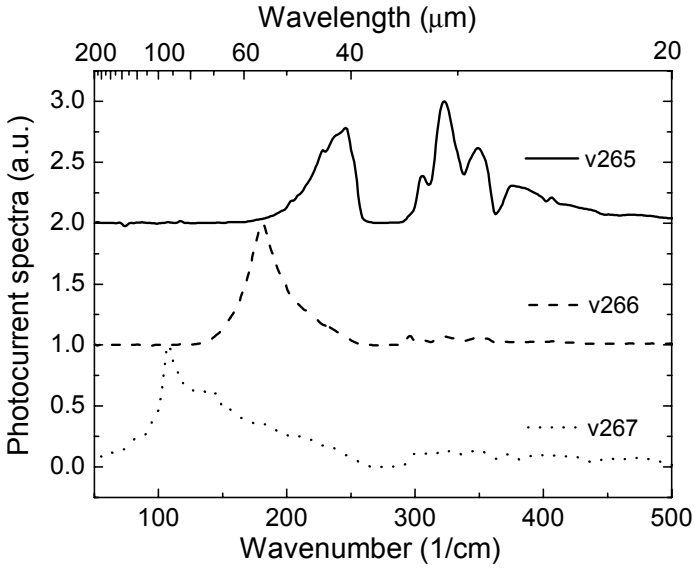

Figure 3: Normalized photocurrent spectra at 8 K. The solid curve is for sample v265 at 0.8 V with a peak response at 322 cm^{-1} (31 μm, 9.7 THz). The dashed curve corresponds to sample v266 at 0.15 V with a peak response at 180 cm^{-1} (56 μm, 5.4 THz). The dotted curve corresponds to sample v267 at 0.03 V with a peak response at 108 cm^{-1} (93 μm, 3.2 THz).

2.2. Experimental results and discussion

Guided by the above design considerations, three test samples were fabricated. The sample parameters are listed in Table I. The wafers were grown by molecular beam epitaxy (MBE) on semi-insulating GaAs substrates. The standard QWIP device consists of a number of GaAs/AlGaAs quantum wells sandwiched between top and bottom contacts.

The barrier thickness was designed so the inter-well tunneling currents are below a certain level (~ 10^{-5} A/cm^2), estimated from Fig. 2. The current level of ~ 10^{-5} A/cm^2 corresponds to the estimated background current. The doping values were chosen to be close to the condition for optimizing detectivity. These values give rise to an estimated absorption in the range of a fraction of percent per well.

Table I: Structure parameters for the THz QWIPs. L_w is the well width, L_b is the barrier width, [Al] is the barrier aluminum fraction, N_d is the Si doping value in the center 10 nm of each quantum well, N is the number of quantum wells, and ν is the frequency corresponding to the calculated intersubband transition energy. The GaAs/AlGaAs MQWs are sandwiched between 400 nm top and 800 nm bottom GaAs contact layers doped with Si to 10^{17} cm^{-3}.

Sample	L_w **(nm)**	L_b **(nm)**	**[Al]**	N_d **(cm^{-3})**	N	ν **(THz)**
v265	11.9	55.2	5%	1×10^{17}	40	7.0
v266	15.5	70.2	3%	6×10^{16}	30	4.2
v267	22.1	95.1	1.5%	3×10^{16}	23	2.2

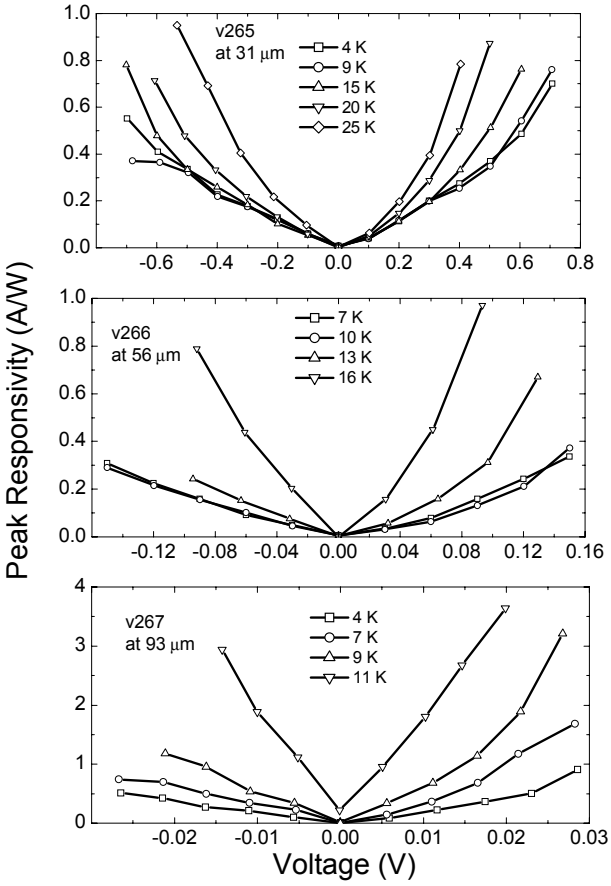

Figure 4: Peak responsivity versus bias voltage at different temperatures for the three THz QWIP samples.

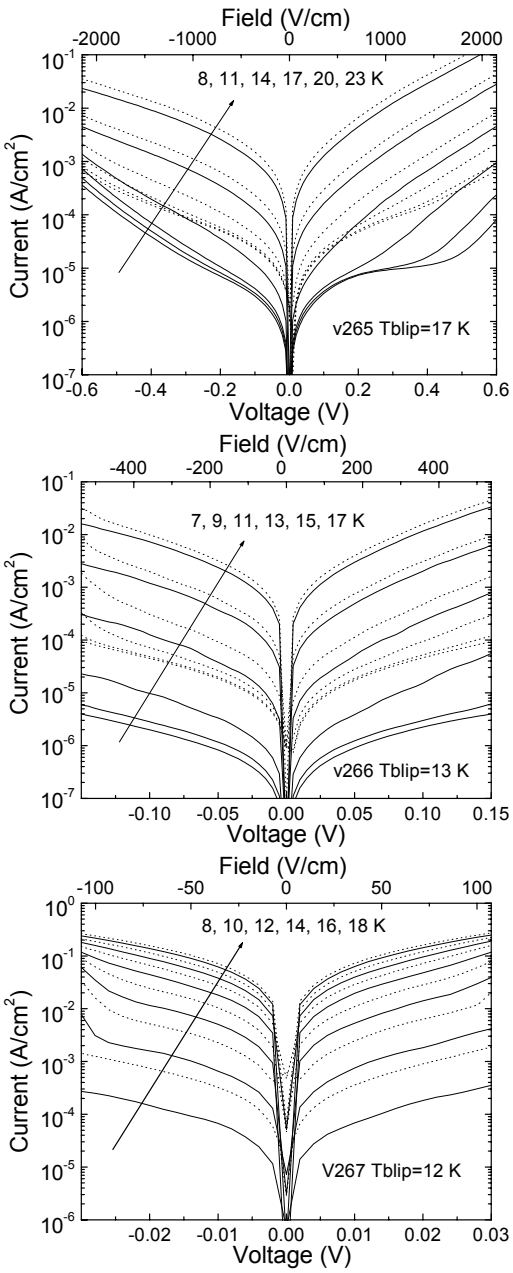

Figure 5: Current voltage curves under dark condition (solid) and under a 90-degree FOV 300 K background (dash).

Mesa devices were fabricated using standard GaAs processing techniques. Test devices were angle polished to give rise to a 45-degree facet and were packaged in the standard double pass backside illumination geometry with a 45-degree internal incidence angle. The photocurrent spectra at 8 K for the three samples are shown in Fig. 3. Photocurrent was observed only under p- polarization, confirming its origin from intersubband transition. The response peaks were measured at 322 cm^{-1} (31 μm, 9.7 THz), 180 cm^{-1} (56 μm, 5.4 THz), and 108 cm^{-1} (93 μm, 3.2 THz) for sample v265, v266, and v267, respectively. These agree reasonably well with the design value, considering the uncertainty in the growth and the untested range of very low aluminum fractions for QWIP design. The main dark region from 265 to 297 cm^{-1} (33 to 37 meV) is due to GaAs optical phonon absorption. Other smaller features are also correlated to AlGaAs phonon and GaAs multi-phonon absorption processes. Due to the strong phonon absorption, the as-observed peak at 322 cm^{-1} for sample v265 has a large uncertainty. The photoresponse spectra for all three samples

are quite broad, indicating that the intersubband transitions are of bound-to-continuum origin. The doping value in the GaAs contact layer (10^{17} cm^{-3}) gives rise to a plasma edge frequency of 101 cm^{-1}, which may contribute to the relatively sharp decline at the longer wavelength side around 100 cm^{-1} for sample v267. For all three samples, the spectral shapes are nearly independent of bias voltage up to a certain voltage value. Beyond the voltage limits, the dark currents increase rapidly and the photocurrent spectra cannot be taken reliably. The voltage limits are ±0.8, ±0.2, and ±0.03 V for sample v265, v266, and v267, respectively.

The calibrated peak responsivity versus bias voltage at different temperatures is shown in Fig. 4. All three responsivity curves show very similar trends. The responsivity increases nearly linearly with bias from the origin, another indication that the transition is of bound-to-continuum origin. The responsivity-voltage curves are almost independent of temperature up to a certain value. Higher than this temperature, the responsivity curves show a marked increase. This upward trend behavior may be related to the increase in mobility with temperature in the impurity scattering limited regime. The responsivity values at low temperature are in the range of 0.4 to 1.0 A/W, comparable to those from mid-infrared and far-infrared QWIPs.[4].

BLIP temperatures were measured by comparing current-voltage curves under dark condition and under a 300 K background with a 90-degree field of view (FOV) at different temperatures. The measured current-voltage curves are shown in Fig. 5. T_{blip} is taken as the temperature at which the background photocurrent equals the dark current. The measured BLIP temperatures are 17, 13, and 12 K for sample v265, v266, and v267, respectively. The results agree reasonably well with the calculated values for v265 and v266 in Fig. 1. For sample v267, the measure value of 12 K is higher than the calculated 5 K. The reason for this is not known presently.

To end this section, working towards a high-performance THz QWIP technology, we have discussed the design parameters and projected characteristics, and presented the experimental results on a set of test device. We have demonstrated BLIP operations of three QWIPs with different detection wavelengths in the terahertz region. Although substantial follow-up work is needed, we are optimistic that we will further improve the performance, and we project that optimized THz QWIPs will be useful for the booming field of THz science and technology.

3. THz QUANTUM-CASCADE LASERS

THz QCL is an exciting area of research and has seen significant progress over the past three years.[6-12] Along with the rapid advances, a good qualitative physical picture of the device operation is emerging, including critical processes such as carrier relaxation, tunneling and dephasing, etc. Based on our current understanding, while we are able to choose the values of most device parameters, we are not able to predict the optimal amount of doping for a given design. In this section, we present a systematic study of the effect of doping on the performance of THz QCLs.

The active region of the QCL wafer, similar to Ref. [11], is based on a 4-well module design in which the THz generating transition is from a pair of anti-crossed double-well states, the longitudinal-optical (LO) phonon mediated relaxation occurs in a wide and doped subsequent well, and the injection to the following double well is from an undoped well. A schematic of the conduction band profile is shown on the left part of Fig. 6, together with the calculated squared wavefunctions of the most relevant states. In order to isolate the effects solely due to doping, it is crucial to keep all the other parameters, including Al fraction and layer (well and barrier) thicknesses, unchanged while varying the doping concentration. A special MBE growth procedure was employed. We used δ-doping with Si at the center of the 153-X-thick "phonon" well and stopped the wafer rotation only during the doping, each time precisely aligning the wafer's $[01\bar{1}]$ crystallographic direction along the Si cell azimuthal orientation (see Fig. 6). This resulted in a nearly linear gradient of the doping concentration across the 3-inch wafer which had otherwise identical layer thicknesses and aluminum fraction. The QCL wafer was grown on a semi-insulating GaAs substrate with 176-cascaded 4-well modules made of GaAs wells and $Al_{0.15}Ga_{0.85}As$ barriers. Cladding and contact layers were the same as those in Ref. [11], except that the etch-stop layer was 0.1-μm-thick AlAs and the lower contact layer was 0.1-μm-thick n^+ GaAs, doped with Si to 5.0×10^{18} cm^{-3}. Beginning with the first injection barrier the layer thicknesses of the 4-well module are **54**/78/**24**/64/**38**/<u>153</u>/**35**/88 X; where the barrier layers are shown in bold and the doped layer is underlined. A schematic of the wafer and the positions of the measured samples are shown on the right part of Fig. 6.

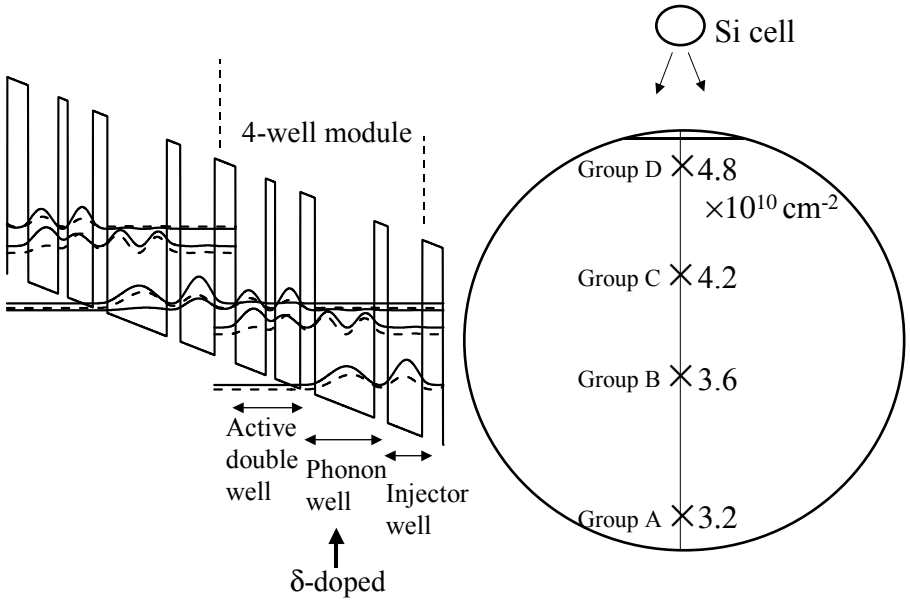

Figure 6: Schematic conduction band profile, calculated wavefunctions, and schematic wafer layout.

Four small pieces (labeled A – D) were used for this study. By secondary ion mass spectroscopy (SIMS) measurements, their δ-doping densities were determined to be 3.2×10^{10} cm^{-2} (Sample A), 3.6×10^{10} cm^{-2} (B), 4.2×10^{10} cm^{-2} (C), and 4.8×10^{10} cm^{-2} (D), respectively. The nearly linear variation across the wafer is in good agreement with theoretical modeling.[13] Doping density and key measured results are listed in Table II. The samples (A to D) were fabricated into high-confinement metal-metal waveguides using In-Au metallic wafer bonding as described in Ref. [11]. Lasers with various ridge widths (ranged from 40 to 200 μm) and cavity lengths (1 – 2 mm) were tested. All lasers were biased in pulsed mode with a pulse width of 1 μs and repetition rate of 1 kHz.

Electrical and optical characteristics of the fabricated QCLs were measured at cryogenic heat-sink temperatures (10 to 120 K). Figure 7(a) shows the temperature-dependent light versus current density curves of one device cut from Sample C. The inset to Figure 7 shows a typical lasing spectrum measured at 10 K, which is peaked at 103.58 μm in wavelength corresponding to 2.9 THz in frequency. Figure 7(b) shows the measured current versus voltage characteristics at various temperatures.

Table II: Doping parameters and measured results. The last two rows list the measured threshold current density at 10 K and in the infinite cavity length limit, and the maximum lasing temperature taken as the mean value of all measured data from each group.

Sample	**A**	**B**	**C**	**D**
δ-doping density (cm^{-2})	3.2×10^{10}	3.6×10^{10}	4.2×10^{10}	4.8×10^{10}
Threshold current density (A/cm^2)	255	408	580	800
Maximum lasing temperature (K)	90	109	88	79

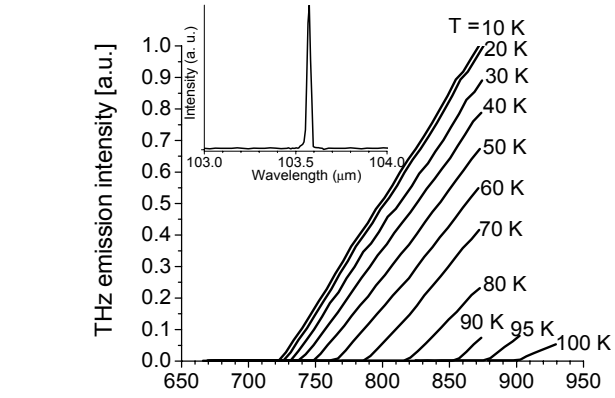

(a)

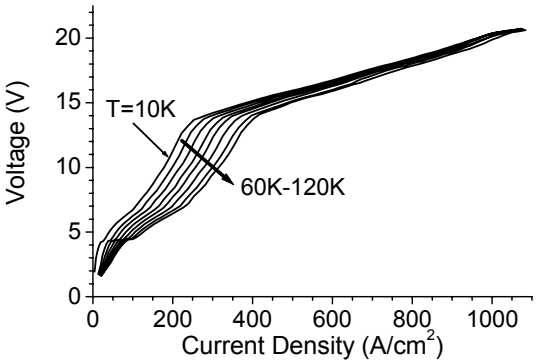

(b)

Figure 7: Lasing light-current (a) and voltage-current (b) curves at different temperatures for a typical QCL device. The inset shows a lasing spectrum. The device was biased at 632 A/cm^2 in pulsed mode (pulse width 1 μs and repetition rate 1 kHz) at 10 K.

Figure 8 shows the threshold current density versus the heat-sink temperature for different groups of devices. Different curves within each group result from devices with different cavity lengths and ridge widths, respectively. The spread represents the uncertainty of this experiment. It is clear that devices with the lowest δ-doping concentration (cleaved from Sample A) have the lowest threshold current density, while J_{th} is the highest for those with the highest δ-doping concentration (Sample D). Figure 9 plots the threshold current density at 10 K for devices with different cavity lengths as a function of the reciprocal cavity length $1/L$. The thresholds in the limit of infinite cavity length ($1/L \rightarrow 0$) are given in Table II. As expected, the threshold current density increases with $1/L$ for all four groups. The behavior in Figs. 8 and 9 is consistent with a monotonic increase of the waveguide loss as the doping concentration is increased. Unfortunately we cannot extract the waveguide loss reliably as it would need an accurate determination of the transparency current density and the parasitic current as well as the mirror loss. For the present metal-metal waveguide, the mirror loss is more complicated to simulate than the usual dielectric waveguide. Recent electro-magnetic simulations of Kohen *et al.* predicted a reflectivity value in the range of 0.76 – 0.85 [14] very different from that of about 0.3 calculated by an effective index of about 3.5.

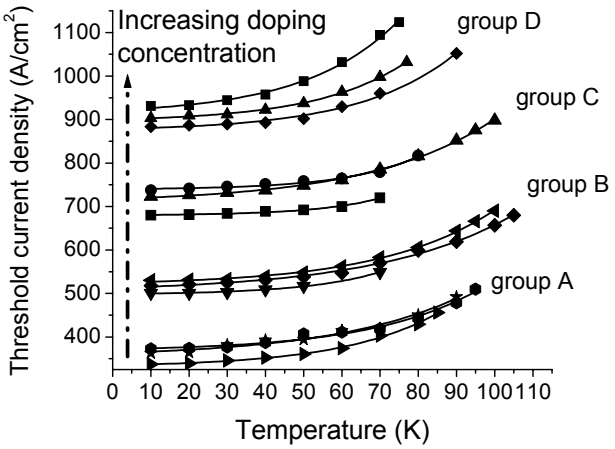

Figure 8: Threshold current density as a function of heat-sink temperature for the four groups of devices with different device dimensions (cavity length and ridge width).

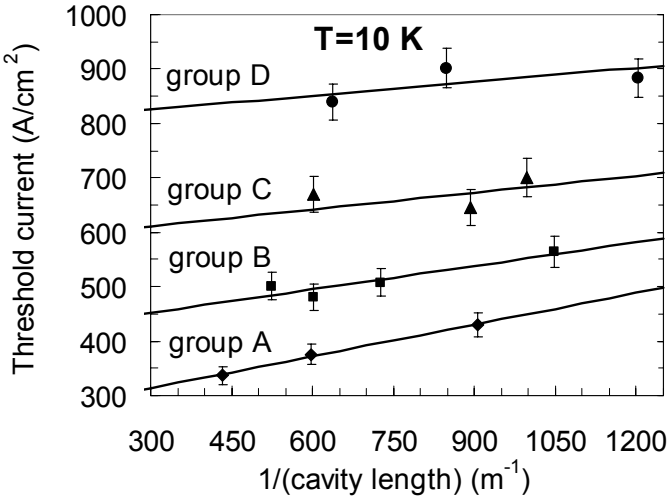

Figure 9: Threshold current density at 10 K as a function of reciprocal cavity length. The symbols show experimental data and the solid lines are linear fits.

Thus far the general trends of the measured results are not surprising: Increasing doping results in an increase in free carrier absorption and waveguide loss and therefore an increase in the threshold current density. It is clear that two extremes of no doping and extremely high doping are of no practical use. There must be an optimum region of doping for certain device characteristics. One of the most important figures of merit is the maximum operating temperature T_{max}, which depends on the range of current densities for which lasing occurs, i.e. $J_{max} - J_{th}$, where J_{max} is the maximum current density for which lasing occurs. Beyond this J_{max}, subband misalignment happens. Increasing the doping concentration increases both J_{th} and J_{max}, but there is an optimum doping which yields the highest T_{max}. Figure 10 shows the observed maximum lasing temperature T_{max} of the four groups of QCLs as a function of δ-doping density. It clearly shows the existence of an optimum δ-doping density (~3.6×10^{10} cm^{-2}) for achieving the highest maximum lasing temperature. Note that each of the experimental points in Fig. 10 is the average of results from several devices and the error bars are the results of a statistical analysis.

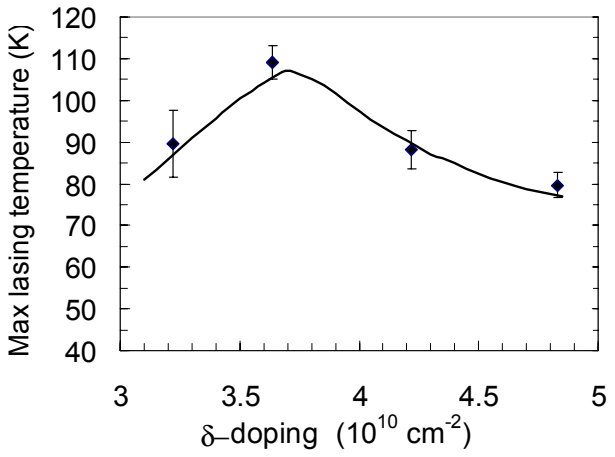

Figure 10: Measured maximum lasing temperature as a function of δ-doping concentration. The maximum temperature was measured in pulsed mode by increasing heat-sink temperature until the lasing operation could not be observed. The symbols are measured results and the line is a guide to the eye.

To conclude, a series of THz QCLs with different δ-doping concentrations in the active region have been fabricated and characterized. Experimental results show that the lasing threshold current density depends strongly on the doping concentration. The results also indicate that the waveguide loss increases with doping. The maximum lasing temperature displays an optimum for a doping density of 3.6×10^{10} cm^{-2}. Our results point out the critical role that the doping concentration plays in reaching high temperature operation.

REFERENCES

1. B. Ferguson and X.-C. Zhang, Nature Materials **1**, 26 (2002).
2. P. H. Siegel, IEEE Trans. Microwave Theory and Techniques **50**, 910 (2002).
3. M. Nagel, P. H. Bolivar, M. Brucherseifer, H. Kurz, A. Bosserhoff, and R. Büttner, Appl. Phys. Lett. **80**, 154 (2002).
4. H. C. Liu, in *Intersubband Transition in Quantum Wells: Physics and Device Applications I*, Academic, San Diego, Semiconductors and Semimetals Vol. 62, 2000, ch. 3, pp. 126-196, edited by H. C. Liu and F. Capasso.
5. H. C. Liu, C. Y. Song, A. J. SpringThorpe, and J. C. Cao , Appl. Phys. Lett. **84**, 4068 (2004).
6. R. Köhler, A. Tredicucci, F. Beltram, H. E. Beere, E. H. Lienfield, A. G. Davis, D. A. Ritchie, R. C. Iotti, and F. Rossi, Nature **417**, 156 (2002).
7. M. Rochat, L. Ajili, H. Willenberg, J. Faist, H. Beere, G. Davies, E. Linfield, and D. Ritchie, Appl. Phys. Lett. **81**, 1381 (2002).
8. B. S. Williams, H. Callebaut, S. Kumar, Q. Hu, and J. L. Reno, Appl. Phys. Lett. **83**, 2124 (2003).
9. B. S. Williams, S. Kumar, H. Callebaut, Q. Hu, and J. L. Reno, Appl. Phys. Lett. **83**, 5142 (2003).
10. R. Köhler, A. Tredicucci, F. Beltram, H. E. Beere, E. H. Linfield, A. G. Davies, D. A. Ritchie, S. S. Dhillon, and C. Sirtori, Appl. Phys. Lett. **82**, 1518 (2003).
11. S. Kumar, B. S. Williams, S. Kohen, Q. Hu, and J. L. Reno, Appl. Phys. Lett. **84**, 2494 (2004).
12. S. Barbieri, J. Alton, H. E. Beere, J. Fowler, E. H. Linfield, and D. A. Ritchie, Appl. Phys. Lett. **85**, 1674 (2004).
13. Z. R. Wasilewski, G. C. Aers, A. J. SpringThorpe, and C. J. Miner, J. Vac. Sci. Technol. B **9,** 120 (1991).
14. S. Kohen, B. S. Williams, and Q. Hu, J. Appl. Phys. **97**, 053106 (2005).